CHAPTER 6
ADSORPTION OF HCN ON Al, Si, AND P-DECORATED C_{18} NANOCLUSTER

6.1.INTRODUCTION

In this chapter, we look into the critical issue of hydrogen cyanide (HCN) exposure, a toxic compound extensively utilized in various industries. Its gaseous form, owing to its low boiling point and high volatility, poses significant risks to workers' health [1]. Preventing environmental contamination is of utmost importance. To address this challenge, researchers have explored the application of carbon-based materials, including pristine or functionalized graphene, carbon nanotubes, graphyne, graphitic carbon nitrides, and silicon carbide nanotubes for HCN sensing. Among these, the C_{18} nanocluster, a novel carbon allotrope, has been the focus of extensive research [2-7]. This nanocluster exhibits strong electron acceptor properties akin to C_{60} and has previously been employed as a sensor for toxic gases [8]. However, our investigation revealed that pristine C_{18} nanocluster exhibits weak physisorption type interaction with HCN molecule, characterized by minimal adsorption energy and large adsorption distances. To enhance this interaction, we introduced Al, Si, and P atoms at various sites of the C_{18} nanocluster aiming to reinforce the affinity between the HCN molecule and $C_{18}X$ (X = Al, Si, P) nanoclusters.

6.2. METHODOLOGY

DFT calculations were conducted on the C_{18} nanocluster using Gaussian 09 package [9], focusing on the range-separated hybrid ωB97XD for its structural geometry. The 6-311++G(d, p) Gaussian basis set was used for all geometry optimizations. The same level of theory was applied to calculate total energies, electronic parameters, work function, recovery time, and adsorption energies. The structural geometry, molecular orbitals, and Mulliken charges were visualized using GaussView, and density of states (DOS) plots were obtained using GaussSum software. The convergence criteria for gradients of root-mean-square (rms) displacement, maximum displacement, rms force, and maximum force were set at 12×10^{-4} radian, 18×10^{-4} Bohr, 3×10^{-4} Hartree/radian, and 45×10^{-5} Hartree/Bohr. The HOMO-LUMO gap (E_G) was calculated to determine the energy difference between the highest occupied molecular orbital (HOMO) and lowest unoccupied molecular orbital (LUMO) [10]:

$$E_G = E_{LUMO} - E_{LUMO} \text{ --- (1)}$$

The Fermi level energy (E_F) is calculated by [11]:

$$E_F = \frac{E_{LUMO}+E_{HOMO}}{2} \text{ --- (2)}$$

6.3. RESULTS AND DISCUSSION

6.3.1. Optimization of HCN molecule and C_{18} nanocluster

First, we optimized the isolated HCN molecule for stability by analysing its structural properties and comparing it to earlier findings using the same ωB97XD/6-311++G(d, p) level theory. The HCN molecule has bond lengths of 1.07 and 1.15 for C-H and C-N bonds, which align with the stated data [12]. H, C, and N atomic charge levels are +0.204e, +0.021e, and -0.226e, respectively. The optimized HCN molecule has a total Mulliken atomic charge value of -0.01e. Then, using the aforementioned computational methods, we optimized the C_{18} nanocluster as well. The alternate lengths for the triple bond and single bond are 1.22 and 1.34, respectively. The HOMO-LUMO energy gap is found to be 6.74 eV, which is consistent with the previous findings [13].

6.3.2. Adsorption properties of HCN molecule over C_{18} nanocluster

We have adsorbed hazardous HCN molecules at various sites of C_{18} nanocluster (on the top of carbon atom, top of triple bond, and top of signal bond) and various orientations of the gas molecules (C/N head of HCN, H head of HCN, and horizontal) at each site of C_{18} nanocluster (on the top of carbon atom, top of triple bond, and top of signal bond). The minimal energy configurations of the HCN molecule are considered for the subsequent calculations. The minimum distance between the nearest C atom of the C_{18} nanocluster and the H atom of the HCN molecule is 3.01, which is quite large, and neither the C_{18} nanocluster nor the HCN molecule undergo structural change.

$$E_{ad} = E(C_{18} + HCN) - E(C_{18}) - E(HCN) \text{ --- (3)}$$

The adsorption energy [14] estimated from equation (3) is -0.24 eV, which is trivial. The optimized geometry of a C_{18} nanocluster before and after HCN adsorption is shown in Figures 6.1(a) and 6.1(b).

Moreover, we calculated the energies of HOMO (Highest Occupied Molecular Orbital), LUMO (Lowest Unoccupied Molecular Orbital), HOMO-LUMO energy gap (E_G), and Fermi level (E_F) to explore the electronic behaviour of adsorption. The energies of HOMO and LUMO after HCN adsorption are -8.53 eV and -1.83 eV, respectively. This means that the value of E_G 6.70 eV is only 0.59% smaller than the original 6.74 eV, and the Fermi level shifts just 0.04 eV lower than the original -5.14 eV [8]. HCN adsorbed C_{18} nanocluster dipole moment increases

by 2.09 Debye. The wide adsorption distance, no change in structural geometry, minor change in HOMO-LUMO gap, and small shift in Fermi level all support the physisorption character of the interaction. Consequently, functionalization provides a possibility for improving the connection between the nanocluster and the molecule. The HOMO and LUMO electron densities of an HCN adsorbed C_{18} nanocluster are depicted in Figure 6.2 (a & b).

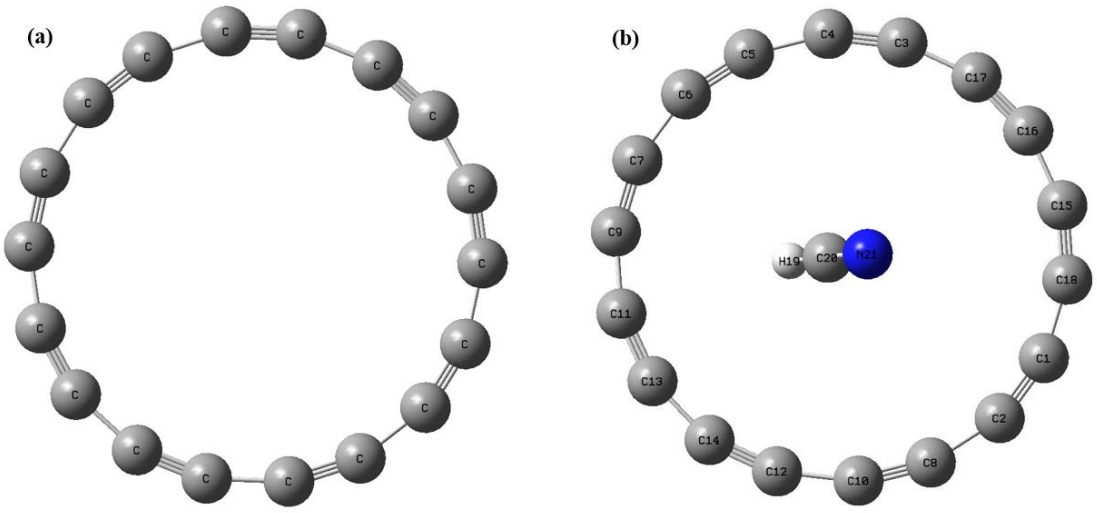

Figure 6.1: Geometrical structure of (a) pristine and (b) HCN adsorbed C_{18} nanocluster

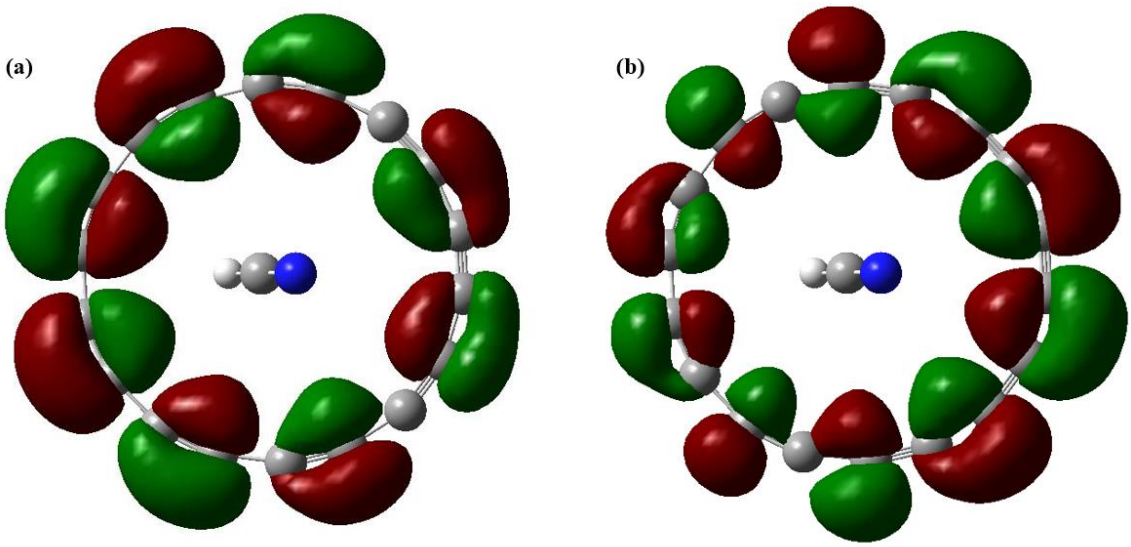

Figure 6.2: (a) HOMO and (b) LUMO electron densities of HCN adsorbed C_{18} nanocluster

6.3.3. Structural Parameters of Al, Si, and P-decorated C_{18} Nanoclusters:

In order to decorate C_{18} nanocluster with Al, Si, and P atoms, our approach involved selecting three distinct sites on the pristine C_{18} nanocluster: the top of a carbon atom, the top of a single bond, and the top of a triple bond. From the three potential configurations available for each Al, Si, and P atom, we identified the most stable arrangement, identified by minimal energy, for subsequent computations.

Our findings revealed noteworthy structural alterations in these decorated nanoclusters. Specifically, the average length of carbon-carbon single bonds extended by 0.02 Å with Al and Si decoration, and by 0.01 Å with P decoration. Conversely, the average length of a triple bond exhibited no substantial change. Furthermore, we calculated the binding distance, denoting the mean separation between the decorated atom and the nearest carbon atom of the C_{18} nanocluster, to be 1.89 Å, 1.83 Å, and 1.81 Å for Al, Si, and P-doped nanoclusters ($C_{18}Al$, $C_{18}Si$, and $C_{18}P$ nanoclusters), respectively. Additionally, alterations in the carbon-carbon-carbon (C-C-C) angles were observed. The average C-C-C angle (θ_1) measured 162.93°, 164.88°, and 162.42° for $C_{18}Al$, $C_{18}Si$, and $C_{18}P$ nanoclusters, respectively. Notably, the C-C-C angle showed significant narrowing in proximity to the decorated atom, represented as θ_2 in our analysis. The corresponding values for θ_2 were 126.94°, 131.26°, and 136.17° for $C_{18}Al$, $C_{18}Si$, and $C_{18}P$ nanoclusters, respectively.

$$E_b = E(C_{18}X) - E(C_{18}) - E(X) \text{ --- (4)}$$

To evaluate the strength of the interaction between the decorated atoms and the nanoclusters, we calculated the binding energies (E_b) [15]. These binding energies were determined by equation (4) as -1.97 eV, -5.19 eV, and -4.45 eV for $C_{18}Al$, $C_{18}Si$, and $C_{18}P$ nanoclusters, respectively. Notably, negative binding energies signify robust interactions between the impurity atoms and the C_{18} nanocluster. Our analysis of the structural parameters, binding lengths, and binding energies for the $C_{18}X$ nanoclusters is presented in Table 1. Additionally, Figure 3(a, b, and c) provides a visual representation of the geometrical structures of $C_{18}Al$, $C_{18}Si$, and $C_{18}P$ nanoclusters.

We computed the formation energy of $C_{18}X$ nanoclusters to assure structural stability [16]:

$$E_{Form} = \frac{E(C_{18}X) - N*E(C) - E(X)}{N+1} \text{ --- (5)}$$

The determined formation energies for $C_{18}Al$, $C_{18}Si$, and $C_{18}P$ nanoclusters are -7.61 eV/atom, -7.77 eV/atom, and -7.74 eV/atom, accordingly. The stability of $C_{18}Al$, $C_{18}Si$, and $C_{18}P$ nanoclusters is indicated by the minus sign of the formation energy.

Table 6.1: Structural parameters (bond length and Angle), binding distance, binding energies of $C_{18}X$ nanocluster

System	Bond length (Å)		Angle		Binding distance (Å)	Binding energy (eV)
	$C-C$	$C \equiv C$	θ_1	θ_2		
C_{18}	1.34	1.22	160.19	159.80	-	-
$C_{18}Al$	1.36	1.22	162.93	126.94	1.89	-1.97
$C_{18}Si$	1.36	1.22	164.88	131.26	1.83	-5.19
$C_{18}P$	1.35	1.22	162.42	136.17	1.81	-4.45

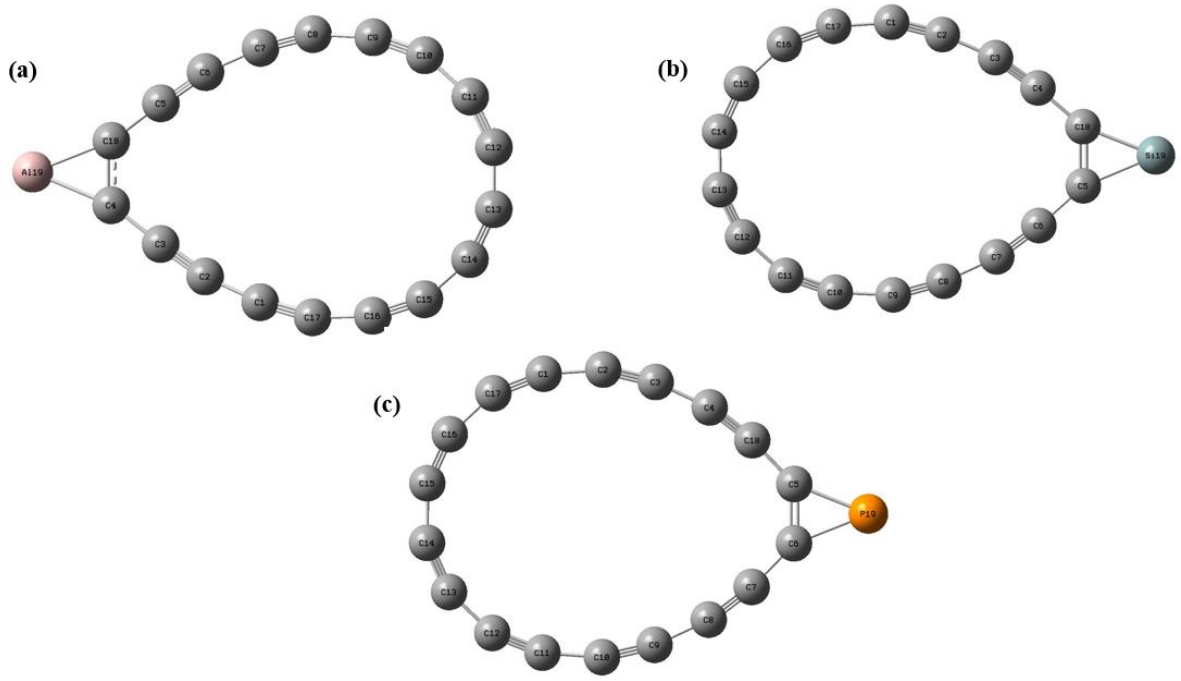

Figure 6.3: Optimized geometries of (a) $C_{18}Al$, (b) $C_{18}Si$ and (c) $C_{18}P$ nanoclusters

6.3.4. Electronic Properties of Al, Si, and P-decorated C_{18} Nanoclusters:

To get into the electronic properties of $C_{18}Al$, $C_{18}Si$, and $C_{18}P$ nanoclusters, we performed comprehensive calculations encompassing E_{HOMO} (Energy of the Highest Occupied Molecular Orbital), E_{LUMO} (Energy of the Lowest Unoccupied Molecular Orbital), HOMO-LUMO energy gap (E_G), and Fermi level (E_F). Notably, our investigation reveals distinctive electronic transformations following Al and P decoration, which lead to the division of

molecular orbitals (MOs) into α-MOs and β-MOs, corresponding to spin-up and spin-down states. For the $C_{18}Al$ nanocluster, we observed a HOMO energy of -7.91 eV for both α and β states, while the LUMO energy was -1.56 eV (α) and -3.18 eV (β). This resulted in an EG of 6.35 eV (α) and 4.73 eV (β), representing a reduction in the energy gap by 5.79% compared to the pristine nanocluster. The Fermi level was identified at -4.73 eV (α) and -5.55 eV (β), and the dipole moment experienced a 5.47 Debye increase. In the case of the $C_{18}Si$ nanocluster, the HOMO and LUMO energies measured -8.16 eV and -1.83 eV, respectively. The Fermi level was situated at -4.99 eV, marking a 0.47 eV elevation compared to the original system. Furthermore, the HOMO-LUMO energy gap diminished by 6.08%, and the dipole moment increased by 2.47 Debye. Lastly, for $C_{18}P$, the HOMO energy reached -7.24 eV (α) and -8.31 eV (β), while the LUMO energy was -2.04 eV (α) and -2.09 eV (β). The resultant E_G equated to 5.15 eV (α) and 6.27 eV (β), indicating a substantial 23.6% reduction in the energy gap when compared to the pristine nanocluster. The Fermi level was identified at -4.67 eV (α) and -5.18 eV (β), while the dipole moment exhibited a 5.47 Debye increase.

Table 6.2: HOMO and LUMO energies (E_{HOMO} and E_{LUMO}), HOMO-LUMO gap (E_G), Fermi level (E_F), change in E_G (ΔE_G), shift in Fermi level (δE_F) and dipole moment (D) of $C_{18}Al$, $C_{18}Si$ and $C_{18}P$ as compared to pristine C_{18} nanocluster.

System	E_{HOMO} (eV)	E_{LUMO} (eV)	E_G (eV)	E_F (eV)	ΔE_G	δE_F (eV)	D (Debye)
C_{18}	-8.51	-1.77	6.74	-5.14	-	-	0.00
$C_{18}Al$	-7.9^{α} -7.91^{β}	-1.56^{α} -3.18^{β}	6.35^{α} 4.73^{β}	-4.73^{α} -5.55^{β}	$-5.79\%^{\alpha}$	+0.41	5.47
$C_{18}Si$	-8.16	-1.83	6.33	-4.99	-6.08%	+0.47	2.47
$C_{18}P$	-7.24^{α} -8.31^{β}	-2.09^{α} -2.04^{β}	5.15^{α} 6.27^{β}	-4.67^{α} -5.18^{β}	$-23.6\%^{\alpha}$	+0.15	0.98

Table 6.2 comprehensively presents E_{HOMO}, E_{LUMO}, E_G, E_F, ΔE_G (Change in E_G), δE_F (Shift in Fermi level), and D (Dipole Moment) values for $C_{18}Al$, $C_{18}Si$, and $C_{18}P$ nanoclusters in comparison to the pristine C_{18} nanocluster. Additionally, Figures 6.4 (a, b, c, d), 5 (a, b), and 6.6 (a, b, c, d) provide visual representations of the electron densities for α-HOMO and LUMO, as well as β-HOMO and LUMO for the respective nanoclusters.

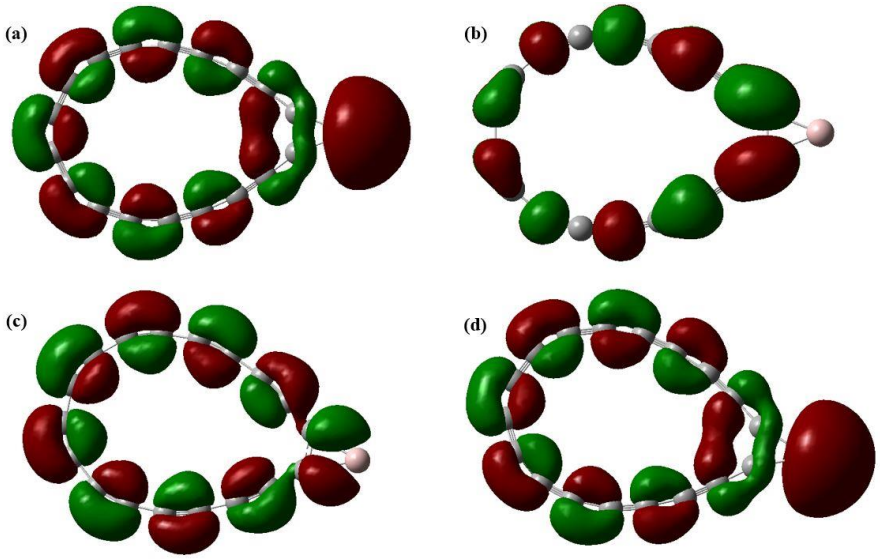

Figure 6.4: (a) α-HOMO (b) α-LUMO (c) β-HOMO (d) β-LUMO electron densities for $C_{18}Al$ nanocluster

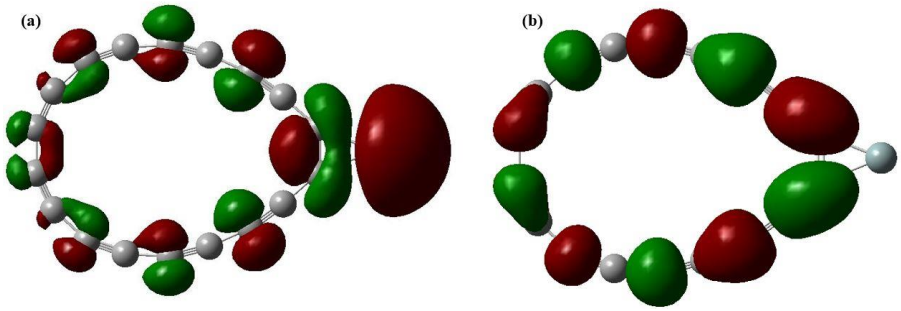

Figure 6.5: (a) HOMO and (b) LUMO electron densities for $C_{18}Si$ nanocluster

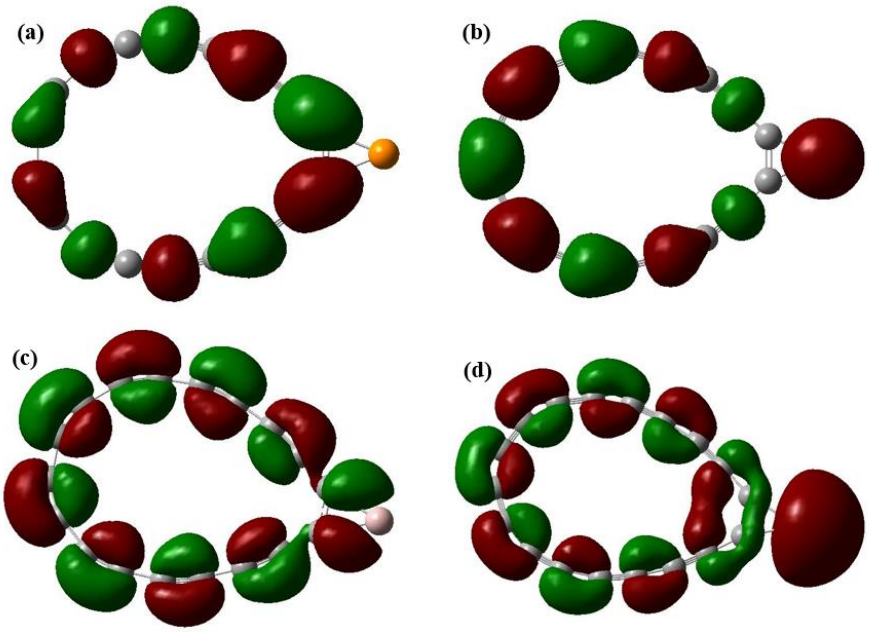

Figure 6.6: (a) α-HOMO (b) α-LUMO (c) β-HOMO (d) β-LUMO electron densities for $C_{18}P$ nanocluster

6.3.5. Adsorption Properties:

Understanding the interaction between the HCN molecule and $C_{18}Al$, $C_{18}Si$, and $C_{18}P$ nanoclusters hinges on the evaluation of adsorption energy. The adsorption energy, as delineated in equation (6), is instrumental in this analysis and is defined as follows:

$$E_{ad} = E(C_{18}X + HCN) - E(C_{18}X) - E(HCN) \text{ --- (6)}$$

Here, X signifies Al, Si, or P, and the terms E(C_{18}X+HCN), E(C_{18}), and E(HCN) correspond to the total energy of the gas-adsorbed $C_{18}X$ nanocluster, the total energy of the $C_{18}X$ nanocluster, and the total energy of the isolated HCN molecule, respectively. To assess the interaction, we have explored three potential adsorption sites for the hazardous HCN molecule on $C_{18}Al$, $C_{18}Si$, and $C_{18}P$ nanoclusters: proximity of the H atom (H-head), C atom (C-head), and N atom (N-head) of the HCN molecule to the dopant atom.

Out of these prospective adsorption configurations, the most stable, denoting minimum energy configurations, have been chosen for further investigation. Notably, for the $C_{18}Al$ nanocluster, the computed adsorption energy, calculated through equation (6), is -0.61 eV, with a minimum adsorption distance of 2.11 Å. In the case of HCN adsorption on the $C_{18}Si$ nanocluster, the adsorption energy amounts to -0.20 eV, while the minimum adsorption distance between the N atom of the HCN molecule and the Si atom of the $C_{18}Si$ nanocluster is 2.83 Å. For $C_{18}P$, the calculated adsorption energy stands at -0.24 eV, with the minimum adsorption distance reaching 3.42 Å. Structural geometries for $C_{18}Al$, $C_{18}Si$, and $C_{18}P$ nanoclusters are visually represented in Figure 8 (a, b, c).

Following HCN adsorption on $C_{18}Al$, the HOMO-LUMO energy gap (E_G) experiences a reduction of 13.1% in the α-spin channel (or a 12.4% increase in the β-spin channel). The Fermi level is situated at -4.73 (α) eV (or -4.79 (β) eV), denoting an upward shift of 0.06 eV. Notably, the dipole moment increases from 5.47 Debye to 12.7 Debye. In the case of HCN adsorption on the $C_{18}Si$ nanocluster, the HOMO and LUMO energies register at -7.97 eV and -1.55 eV, respectively. The HOMO-LUMO energy gap (E_G) experiences a modest increase of 1.42%, while the Fermi level rises to -4.76 eV, indicating a 0.23 eV upward shift. Similarly, the dipole moment increases from 2.47 Debye to 5.33 Debye. In the scenario of HCN adsorption over $C_{18}P$, the HOMO-LUMO energy gap (E_G) shows an increase of 7.38% in the α-spin channel (or a decrease of 3.35% in the β-spin channel). The Fermi level is situated at -5.15 (α) eV (or -5.53(β) eV), signifying a 0.38 eV upward shift. The dipole moment experiences an increase from 0.98 Debye to 2.44 Debye.

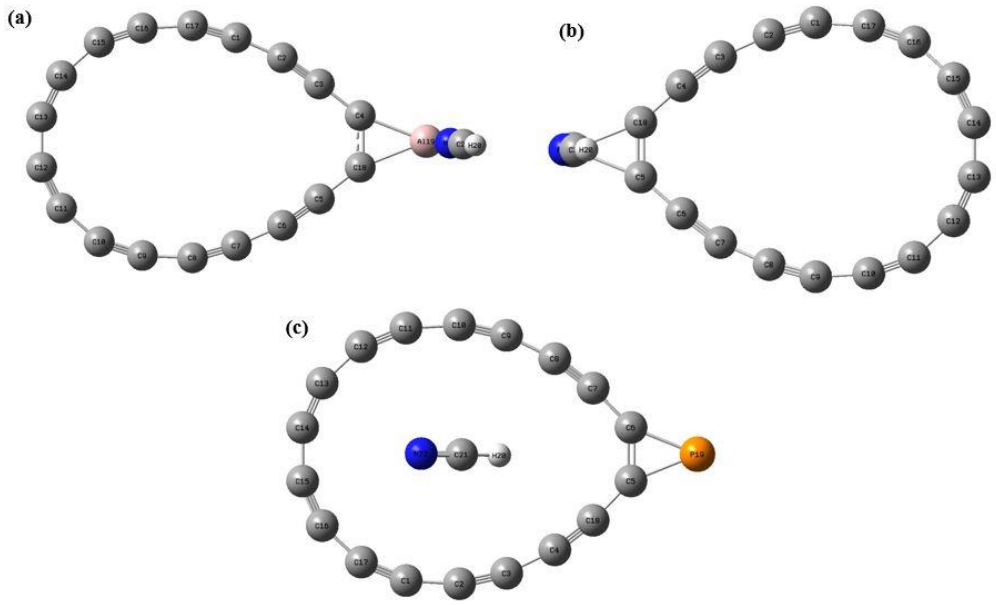

Figure 6.7: Structural geometries of HCN adsorbed (a) $C_{18}Al$ (b) $C_{18}Si$ and (c) $C_{18}P$ nanoclusters

Table 6.3 presents a comprehensive overview of the adsorption energies (E_{ad}), HOMO and LUMO energies (E_{HOMO} and E_{LUMO}), Fermi level (E_F), shift in Fermi level (δE_F), HOMO-LUMO gap (E_G), change in E_G (ΔE_G), adsorption distance (d), and dipole moment (D) for HCN adsorbed on $C_{18}Al$, $C_{18}P$, and $C_{18}Si$ nanoclusters in comparison to HCN adsorbed on the pristine C_{18} nanocluster. Furthermore, Figure 6.8 (a, b, c, d), Figure 6.9 (a, b), and Figure 6.10 (a, b, c, d) visually represent the α-HOMO and LUMO, as well as the β-HOMO and LUMO electron densities for HCN adsorbed on $C_{18}Al$, $C_{18}Si$, and $C_{18}P$ nanoclusters.

Table 6.3: adsorption energies (E_{ad}), HOMO and LUMO energies (E_{HOMO} and E_{LUMO}), Fermi level (E_F), shift in Fermi level (δE_F), HOMO-LUMO gap (E_G), change in E_G (ΔE_G), adsorption distance (d) and dipole moment (D) of HCN adsorbed $C_{18}Al$, $C_{18}P$, $C_{18}Si$, as compared to HCN adsorbed pristine C_{18} nanocluster.

System	E_{ad} (eV)	E_{HOMO} (eV)	E_{LUMO} (eV)	E_G (eV)	E_F (eV)	ΔE_G	δE_F (eV)	d (Å)	D (Debye)
HCN/C_{18}	-0.24	-8.53	-1.83	6.70	-5.18	-0.59%	-0.04	3.03	2.09
HCN/$C_{18}Al$	-0.61	-7.49^{α} -7.49^{β}	-1.97^{α} -2.09^{β}	5.52^{α} 5.40^{β}	-4.73^{α} -4.79^{β}	$-13.1\%^{\alpha}$ $12.4\%^{\beta}$	0^{α} $+0.76^{\beta}$	2.11	12.7
HCN/$C_{18}Si$	-0.20	-7.97	-1.55	6.42	-4.76	1.42%	+0.23	2.83	5.33
HCN/$C_{18}P$	-0.24	-7.91^{α} -8.56^{β}	-2.38^{α} -2.50^{β}	5.53^{α} 6.06^{β}	-5.15^{α} -5.53^{β}	$7.38\%^{\alpha}$ $-3.35\%^{\beta}$	-0.48^{α} -0.35^{β}	3.42	2.44

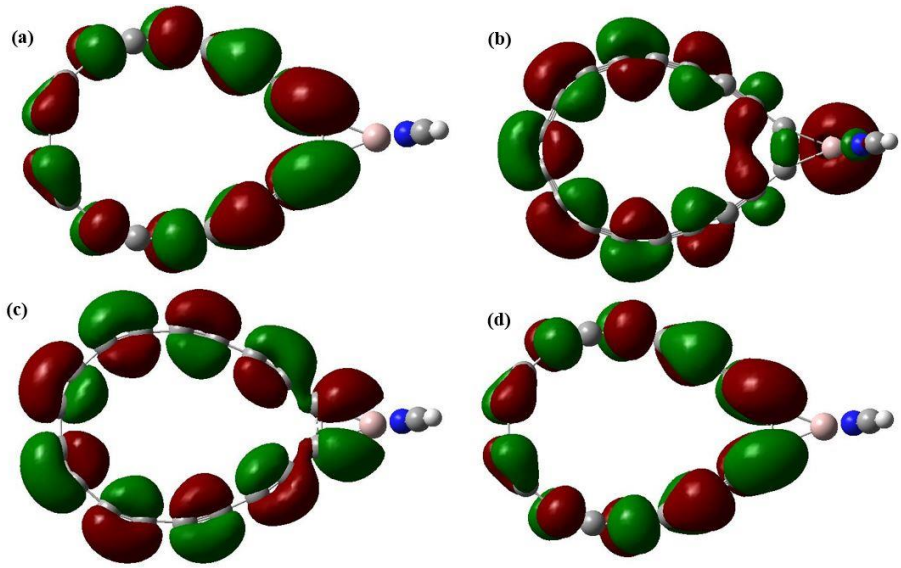

Figure 6.8: (a) α-HOMO (b) α-LUMO (c) β-HOMO (d) β-LUMO electron densities for HCN adsorbed $C_{18}Al$ nanocluster

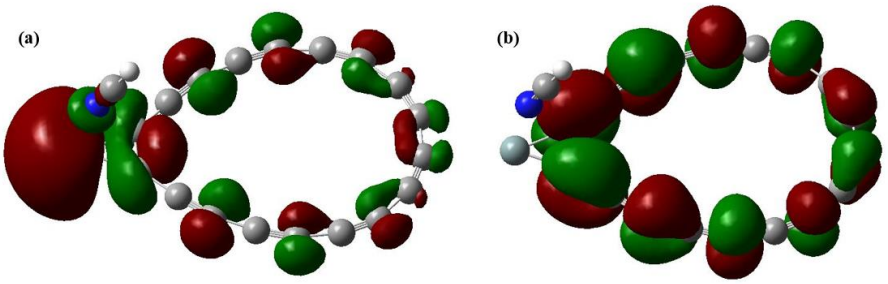

Figure 6.9: (a) HOMO and (b) LUMO electron densities of HCN adsorbed $C_{18}Si$ nanocluster

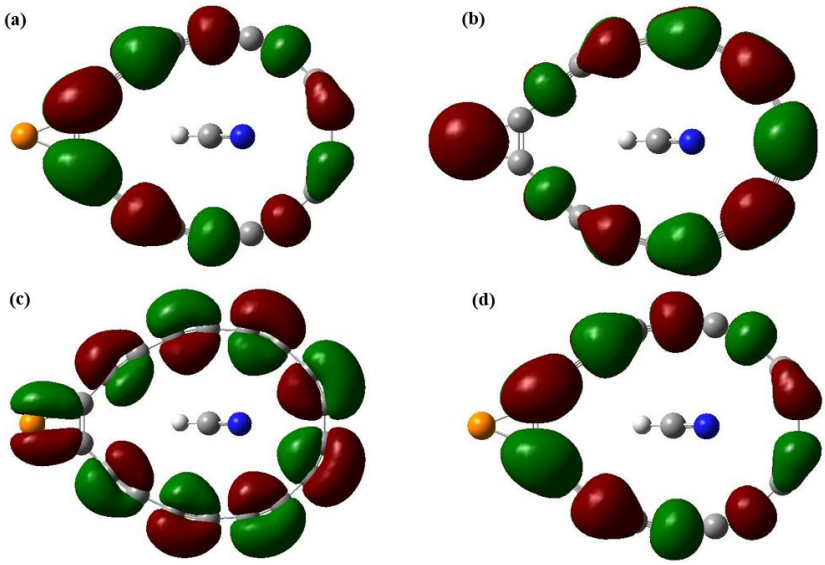

Figure 6.10: (a) α-HOMO (b) α-LUMO (c) β-HOMO (d) β-LUMO electron densities for HCN adsorbed $C_{18}P$ nanocluster

6.3.6. Mulliken Charge Transfer Analysis

Charge transfer is always possible due to the interaction of HCN molecules with C_{18}, $C_{18}Al$, $C_{18}Si$, and $C_{18}P$ nanoclusters. Mulliken charge population [17] is used to assess the charge transfer. The total Mulliken charge on an HCN molecule after adsorption is -0.042e, +0.245e, +0.027e, and -0.109e for C_{18}, $C_{18}Al$, $C_{18}Si$, and $C_{18}P$ nanoclusters, respectively. This implies that charge transfer is occurring from C_{18} and $C_{18}P$ nanoclusters to HCN molecules, as isolated HCN molecules have a total charge of -0.01e. Charge transfer from gas molecules to $C_{18}Al$, $C_{18}Si$ nanoclusters occurs in the other two scenarios [18]. Figure 6.11 depicts the charge distribution of the gas adsorbed C_{18} nanocluster.

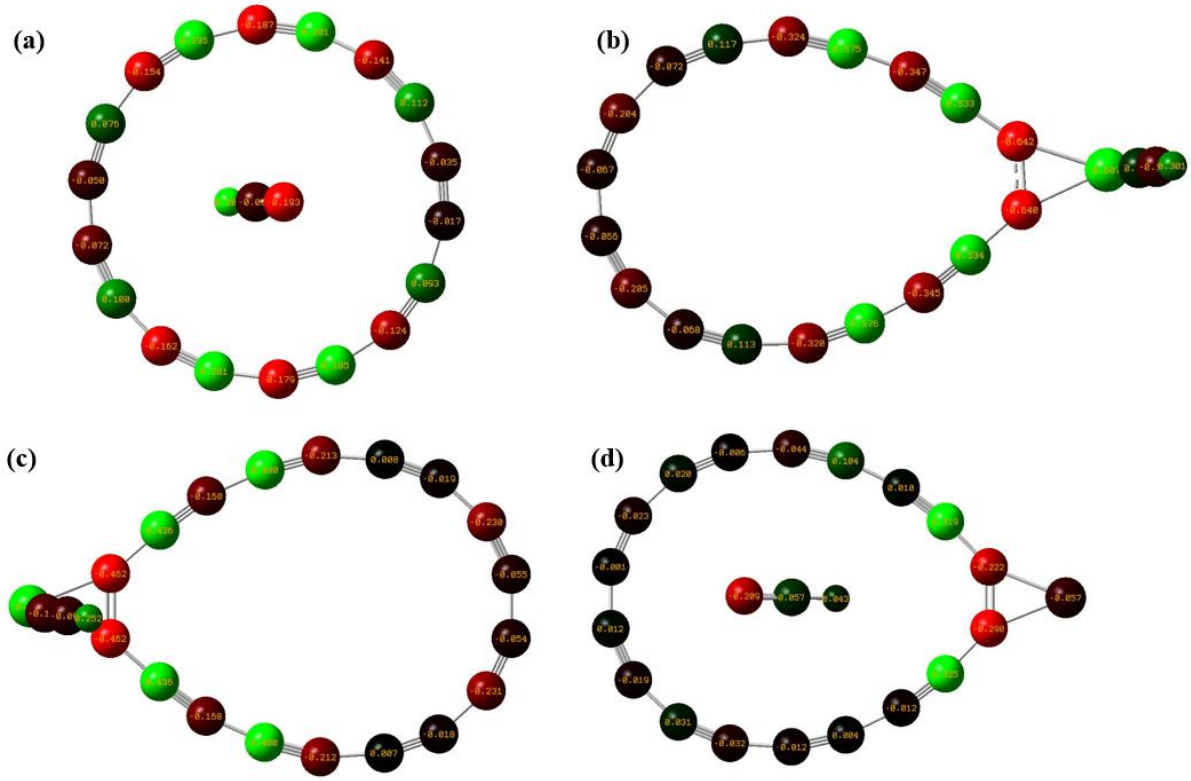

Figure 6.11: Mulliken atomic charge distribution of the HCN adsorbed (a) C_{18}, (b) $C_{18}Al$, (c) $C_{18}Si$, and (d) $C_{18}P$ nanoclusters respectively

6.3.7. Sensing Properties

Gas adsorption significantly impacts the Fermi level and work function (φ) of materials, making it a critical consideration for φ-type sensors. These sensors utilize a Kelvin oscillator instrument to estimate φ values both before and after the adsorption of gas molecules. Alterations in the φ due to gas adsorption lead to fluctuations in the gate voltage, resulting in the generation of an electrical signal [19]. The work function (φ) represents the minimum

energy required to extract an electron from a material to a point just outside the solid surface within a vacuum. It can be calculated using the following equation [20]:

$$\varphi = V_{el(+\alpha)} - E_F \quad \text{--- (7)}$$

where $V_{el}(+\alpha)$ and E_F denote the electrostatic potential energy far from the material's surface and the Fermi energy, respectively. When $V_{el}(+\alpha)$ is equal to zero, φ can be expressed as $-E_F$ based on Equation (6). The changes in the φ value during the gas adsorption process of an adsorbent system can impact its field emission characteristics. This relationship can be correlated using the classical Richardson-Dushman equation, which describes the current density of emitted electrons in a vacuum as follows [21]:

$$j = AT^2 \exp\left(-\frac{\varphi}{kT}\right) \quad \text{--- (8)}$$

Here, A represents the Richardson constant (A/m^2), and T signifies the temperature.

Following HCN adsorption, interactions between the molecule and C_{18}, $C_{18}Al$, $C_{18}Si$, and $C_{18}P$ nanoclusters result in variations in the HOMO and LUMO energies of these nanoclusters. These alterations in HOMO and LUMO energies lead to changes in the work function, as indicated in Table 4. The work function increases by 0.78% after HCN interacts with C_{18}. For $C_{18}Al$, interaction with HCN does not induce a change in α-MOs but causes a 13.7% reduction in β-MOs. In the case of $C_{18}Si$ nanoclusters, the work function decreases by 4.61% following adsorption. However, for HCN adsorption over $C_{18}P$, the work function increases by 10.3% in the α-spin channel (or 6.76% in the β-spin channel). Our findings suggest that both $C_{18}Al$ (specifically for β-MOs) and $C_{18}Si$ nanoclusters may serve as φ-type sensors for HCN molecules since they exhibit a decrease in φ. Nevertheless, it's worth noting that HCN molecules show physisorption, indicating the unsuitability of these nanoclusters for φ-type sensor applications.

Table 6.4: Work function(φ), change in work function ($\Delta\varphi$), recovery time (τ) of HCN adsorbed C_{18}, $C_{18}Al$, $C_{18}Si$, $C_{18}P$ nanoclusters respectively.

System	φ (eV)	$\Delta\varphi$	τ (s)
HCN/C_{18}	5.18	0.78%	1.08×10^{-8}
HCN/$C_{18}Al$	4.73^{α} 4.79^{β}	0% -13.7%	0.0177
HCN/$C_{18}Si$	4.76	-4.61%	2.29×10^{-9}
HCN/$C_{18}P$	5.15^{α} 5.53^{β}	10.3% 6.76%	1.08×10^{-8}

Another essential parameter for gas molecule sensors is the recovery time, which can be defined as the anticipated duration required for an adsorbed molecule to desorb or detach from its host system. In the context of gas sensors, shorter recovery times are preferable as they indicate more efficient performance. A strong interaction between gas molecules and the sensor, on the other hand, can be detrimental for the sensor's performance. This is because the desorption process of gas molecules becomes challenging, leading to longer recovery times.

The formula used to calculate the recovery time [22] is as follows:

$$\tau = \upsilon^{-1} \exp(\frac{-E_{ad}}{kT}) \text{ --- (9)}$$

In this equation, τ represents the recovery time, υ is the attempt frequency, E_{ad} is the adsorption energy, k is the Boltzmann constant, and T is the temperature. In our calculations, we have chosen an attempt frequency of 10^{12} s^{-1} and a room temperature of 300 K. The computed recovery time for HCN adsorbed on C_{18} and $C_{18}P$ nanoclusters is 10.8 ns. However, for the interaction of HCN with $C_{18}Al$ and $C_{18}Si$ nanoclusters, the recovery times are 17.7 ms and 2.29 ns, respectively. These results indicate that $C_{18}Al$ nanoclusters are the most suitable candidates for HCN sensors in terms of recovery time.

6.4. CONCLUSION

In this chapter, we have employed density functional theory to investigate the structural, electronic, and molecular adsorption characteristics of HCN on C_{18}, $C_{18}Al$, $C_{18}Si$, and $C_{18}P$ nanoclusters. The pristine C_{18} nanocluster exhibits physisorption behavior when interacting with the HCN molecule, characterized by a large adsorption distance of 3.01 Å and a negligible adsorption energy of -0.24 eV. To enhance the adsorption performance, we introduced dopants (decorative atoms) in the form of Al, Si, and P. The decorated nanoclusters displayed negative binding energy and negative formation energy, indicating a strong interaction between the dopants and the C_{18} nanocluster, ensuring structural stability. However, it's worth noting that the $C_{18}Al$, $C_{18}Si$, and $C_{18}P$ nanoclusters also exhibit physisorption behavior when interacting with the HCN molecule. Among these, the adsorption energy of the HCN molecule on $C_{18}Al$ is noteworthy (-0.61 eV), and it features a short adsorption distance of 2.11 Å. Notably, $C_{18}Al$ boasts a recovery time of 17.7 ms, making it the most suitable candidate for an HCN sensor among the nanoclusters discussed.

BIBLIOGRAPHY:

[1] D. R., J. R., A. Verma, B. C. Choudhary and R. K. Sharma, *Comput. Theor. Chem.*, 2022, **1209**, 21–26.

[2] R. Deji, B. C. Choudhary and R. K. Sharma, *Phys. E Low-Dimensional Syst. Nanostructures*, 2021, **134**, 114844.

[3] T. Zhang, S. Mubeen, N. V. Myung and M. A. Deshusses, *Nanotechnology*, 2008, **19**, 1–2.

[4] Z. Lu, P. Lv, D. Ma, X. Yang, S. Li and Z. Yang, *J. Phys. D. Appl. Phys.*, 2021, **51**, 065109.

[5] H. Basharnavaz, A. Habibi-Yangjeh and M. Pirhashemi, *Chem. Phys. Lett.*, 2020, **754**, 137676.

[6] M. V. Nikolic, V. Milovanovic, Z. Z. Vasiljevic and Z. Stamenkovic, *Sensors (Switzerland)*, 2020, **20**, 1–31.

[7] K. Kaiser, L. M. Scriven, F. Schulz, P. Gawel, L. Gross and H. L. Anderson, *Science (80-.).*, 2019, **365**, 1299–1301.

[8] S. Vadalkar, D. Chodvadiya, N. N. Som, K. N. Vyas, P. K. Jha and B. Chakraborty, *ChemistrySelect*, 2022, **7**, e202103874.

[9] M. J. Frisch, Trucks, G.W., Schlegel, H.B., Scuseria, G.E., Robb, M.A., Cheeseman, J.R., *Gaussian 09, Revis. A.02, Gaussian, Inc.*, 2016, 1–2.

[10] N. R. Sheela, S. Muthu and S. Sampathkrishnan, *Spectrochim. Acta - Part A Mol. Biomol. Spectrosc.*, 2014, **120**, 237–251.

[11] M. Sharma, P. Jamdagni, A. Kumar and P. K. Ahluwalia, *AIP Conf. Proc.*, 2016, **1731**, 10–13.

[12] S. Vadalkar, D. Chodvadiya, K. N. Vyas and P. K. Jha, *Mater. Today Proc.*, 2022, **67**, 229–237.

[13] A. J. Stasyuk, O. A. Stasyuk, M. Solà and A. A. Voityuk, *Chem. Commun.*, 2020, **56**, 352–355.

[14] S. Patel, P. Patel, D. Chodvadiya, N. N. Som and P. K. Jha, *J. Mol. Liq.*, 2022, **352**,

118702.

[15] A. S. Rad, S. M. Aghaei, E. Aali and M. Peyravi, *Diam. Relat. Mater.*, 2017, **77**, 116–121.

[16] S. Vadalkar, D. Chodvadiya, N. N. Som, K. N. Vyas and P. K. Jha, *ChemistrySelect*, 2023, **8**, e202204862.

[17] R. S. Mulliken, *J. Chem. Phys.*, 1935, **3**, 586–591.

[18] Z. Wu, J. Zhou, D. Li, Z. Ao, T. An and G. Wang, *Sustain. Mater. Technol.*, 2021, **29**, e00294.

[19] K. Patel, B. Roondhe, S. D. Dabhi and P. K. Jha, *J. Hazard. Mater.*, 2018, **351**, 337–345.

[20] J. Mawwa, S. U. D. Shamim, S. Khanom, M. K. Hossain and F. Ahmed, *RSC Adv.*, 2021, **11**, 32810–32823.

[21] Y. Liu, C. Liu and A. Kumar, *Mol. Phys.*, 2020, **118**, 1–8.

[22] S. Peng, K. Cho, P. Qi and H. Dai, *Chem. Phys. Lett.*, 2004, **387**, 271–276.